Advances in Aerodynamics

RESEARCH Open Access

Aerodynamic analysis of a generic wing featuring an elasto-flexible lifting surface

J. Piquee*, I. López Canalejo, C. Breitsamter, R. Wüchner and K.-U. Bletzinger

*Correspondence:
julie.piquee@aer.mw.tum.de
Technische Universität München, Boltzmannstraße 15, 85748 Garching bei München, Germany

Abstract

A three-dimensional-membrane-type wing is investigated applying fluid-structure-interaction computations and complementary experiments. An analysis for three Reynolds numbers is conducted at various angles of attack. The computations are performed by means of the TAU-Code and the FEM Carat++ solver. Wind-tunnel tests are carried out for performance analysis and to estimate the accuracy of the computations. In the results, the advantages of an elasto-flexible-lifting-surface concept are highlighted by comparing the formvariable surface to its rigid counterpart. The flexibility of the material and its adaptivity to the freestream allow the membrane to adjust its shape to the pressure distribution. For positive angles of attack, the airfoil's camber increases resulting in an increase in the wing lifting capacity. Furthermore, the stall onset is postponed to higher angles of attack and the abrupt decrease in the lift is replaced by a gradual loss of it.

Keywords: Morphing systems, Elasto-flexible membrane wing, Fluid-structure-interaction, Experimental data

1 Introduction

Shape adaptivity during flight can offer great potential in different domains of the aerodynamics of an aircraft [1–4]. In recent years, adaptivity has been under the scope of various research studies behind the word *morphing*. Morphing aircraft are able to transform their configuration by using shape-adaptive systems: They can refer to a change in the outer shape or in the inner structure, but it can also involve a change in the noise and the electromagnetic signature. The main purpose of such a system is to increase flight efficiency and expand flight envelopes; i.e., a single aircraft can be used for various types of missions.

1.1 Morphing aircraft systems

There has been a growing trend toward morphing systems in the aerodynamics of aircraft over the last decade. Various examples could be enumerated to show the advantages of such systems. With regards to aircraft, one instance is a variable wing-sweep system used in the NextGen MFX-1 [5]. The aircraft is designed with a wing using an innovative flexible skin, allowing the wing to smoothly change its shape. The wing area and the sweep angle are interdependent. The dependency between the wing area, the wing span, the wing chord and the wing sweep permits to combine an efficient loiter configuration with a high-speed dash configuration by morphing the wing from a high- to a

low-aspect ratio. Another instance is a variable camber wing system realized with a modification of the thickness. The flexibility and adaptivity of an anisotropic material such as a membrane could be exploited to change the thickness of an airfoil. The shape of the wing adapts to both the freestream velocity (dynamic pressure) and the angle of attack, and depends on the pretension of the membrane. A deformation of the membrane varies the thickness and, thus, varies the aerodynamic properties. Research on membrane wings is quite common with respect to MAVs [6–9] but also with regards to aircraft [10, 11]. Aerodynamic force measurements indicate that a flexible-membrane system renders better aerodynamic performances compared to a rigid wing [6]. The flexibility resulted in a natural adaptation of the shape to the flow through a softer stabilization of the pressure difference between the upper and the lower side of the wing. Consequences of the adaptation are an increase in the lift coefficient, while the onset of stall is shifted to higher angles of attack [6].

1.2 Wind turbine adaptive means

Flexibility offers advantages with regards to aircraft but should be exploited to high-Reynolds-number-operating machines as well. Wind energy technology has been in the scope of scientific research due to environmental concerns [12]. The wind-turbine size has been continuously increasing to improve the performance of the system over the past years. Therefore, new technologies are required to enable the feasibility of bigger rotors with a special focus on structural issues. Reducing fatigue loads induced from aerodynamics appears necessary. Many studies are focusing on developing new technologies also named as 'smart structure' or 'smart rotor control' enabling reduction loads on a blade. It can be thought of various concepts already investigated in helicopter systems. Nevertheless, an increase in weight, in complexity or in moving parts should be restrained as the maintenance still needs to be limited. Furthermore, it is more interesting to control the loads on the blade roots, which naturally implies to use small devices near the tip blade because of the lever arm. Flaps or microtabs seem promising to be located at the tip blade [13–16]. They could be used as discrete devices or as continuous deformable trailing edge. Both systems alter the pressure distribution on the blade and offer an enhancement or a mitigation in lift, which directly affect the aerodynamic load on the blade. The paper at hand focuses on a variable-camber wing made with an elasto-flexible membrane as lifting surface. Such a concept was already investigated in the aircraft sector and shows a great potential in tailoring aerodynamic loads. Hence, an extension of this morphing concept to high-Reynolds-number-operating machines suggests itself. The concept appears as an interesting solution when it is taken as a part of the blade tip section. Altering the shape of the blade tip area by means of a membrane section without adding additional weight may be a powerful concept which needs to be investigated.

1.3 Fluid-structure interaction computations for morphing systems

In spite of the numerous potential advantages of adaptivity on aerodynamic characteristics and efficiency, the capability of morphing systems still needs to be explored. A key aspect is represented by high-fidelity computations able to accurately predict the behavior of such systems. Fluid-Structure-Interaction (FSI) computations were employed to investigate the fish-bone-active-camber morphing concept [11]. The FSI computations used two codes to separately investigate the aerodynamics and the structural mechanics

of the system. The aerodynamic pressure was found with the XFOIL panel-method code using a boundary-layer coupling, while the deflections of the trailing edge were computed with an Euler-Bernoulli beam-theory-based analysis. These codes were coupled and iterated until convergence was achieved for the relevant parameters [11]. A two-level optimization routine was also investigated for morphing camber airfoil [17]. The XFOIL code was used for the aerodynamic analysis whereas a Finite Volume Beam elements method was used for the structural analysis. A genetic algorithms was finally developed to find the best airfoil change and the best structural configuration to satisfy the requirements.

Elasto-flexible membrane systems are controlled by a strong reciprocity between the membrane's deformation and the pressure distribution. Therefore, FSI computations are needed as well to analyze the system. The current paper presents a FSI investigation of an elasto-flexible membrane wing/airfoil. The Reynolds-averaged-Navier-Stokes (RANS) code TAU from the German Aerospace Center (DLR) [18] and the finite-element method (FEM) CARAT++ from the Chair of Structural Analysis at Technical University of Munich (TUM-SA) [19] are employed. Comparison with experimental data allows to evaluate the validity of the computations, and eventually leads to an assessment of the passive-camber-change concept.

2 Elasto-flexible membrane wing model

2.1 Geometry conception

Acting on the flow at the tip blade should have a more important impact on the loads at the root because of the lever arm. The configuration investigated in the current study is a half-type three-dimensional-elasto-flexible-membrane wing. The geometry is tapered as it can properly represent the advantages of such a concept when it is located at the blade tip area. It was decided not to use a twist in order to focuse the study only on the influence of the membrane. The wing is made of two rigid spars, the first one along the leading-edge (LE) and the second one along the trailing-edge (TE). The lifting surface is a highly tensioned, anisotropic elastic fabric sewed onto the two spars. The membrane is coated on the outside of the wing with a rubber layer to ensure air impermeability. The mechanical properties were determined with uniaxial tensile tests on membrane material samples. The moduli of elasticity are $E_1 = 2.1$ MPa and $E_2 = 4$ MPa in the warp and weft directions, respectively. The chord direction aligns to the weft direction to limit the deformation of the membrane when it is loaded. The lift of the wing increases with an increase of the camber. However, a too strong increase in camber eventually leads to flow separation.

The wing geometry is depicted in Fig. 1. The LE spar has been designed in [20, 21]. Its shape is a double ellipse, which permits a reduction of the suction peak of the resulting pressure distribution on the wing upper side. The various lengths are also shown. Two sketches describe the geometry of the airfoils used for the wing: Section A-A represents the airfoil geometry for the inboard part of the wing and section B-B represents the airfoil geometry at the outboard part of the wing. The TE spar is a cylinder and was constructed as adjustable to pre-stress the membrane. The TE can be translated in the chordwise direction to introduce an initial elongation. In the current study, a pre-strain of 10% of the chord length is set on the membrane. The initial pre-strain corresponds to an initial of pre-stress $\sigma_0 = 2.1$ MPa.

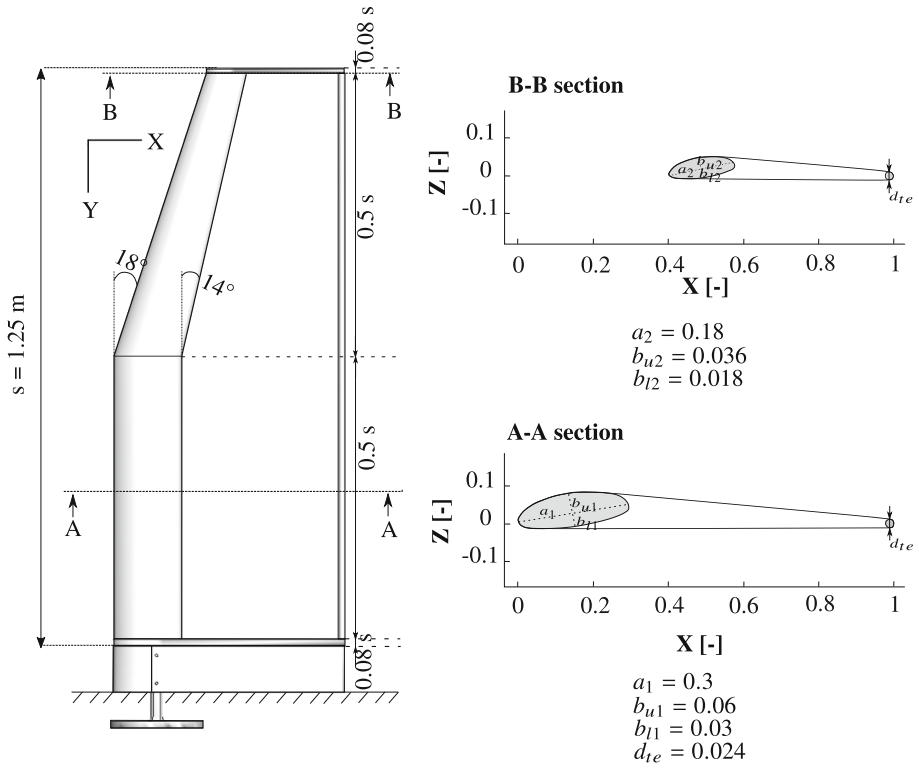

Fig. 1 Three dimensional elasto-flexible membrane wing model with geometrical characteristics

The impermeability of the configuration is necessary to ensure meaningful results during the wind-tunnel tests. Therefore, two rigid blades were included at the root and the tip of the wing. The blades have the same geometry as the root and the tip airfoil geometry (Section A-A and B-B of Fig. 1) of the wing and allowed to seal the membrane at them. The tip wing has been designed with a taper ratio of $\lambda = 0.6$, which results in a wing reference area of $S = 0.564\ \mathrm{m}^2$ and an aspect ratio of $AR = 3.26$.

2.2 Experimental configuration

The experimental configuration of the elasto-flexible membrane wing is represented in Fig. 2. The wing is mounted in the test section of the wind tunnel A of the Chair of Aerodynamics and Fluid Mechanics at the Technical University of Munich (TUM-AER). A peniche, represented in Fig. 1, with the same geometry as the airfoil at the wing root is placed under the wing to avoid any influences of the boundary layer of the wind-tunnel test section floor. Both the peniche and the wing are mounted on a circular plate in the test section, which can be rotated to set the angle of attack α. The wing is directly connected to an aerodynamic balance under the wind-tunnel test section floor to measure forces and moments. There is no contact between the peniche and the wing, ensuring that the balance only measures the aerodynamic forces and moments acting on the wing.

In addition to aerodynamic force and moment measurements, photogrammetry tests were performed to measure the deformation of the membrane. More information about both techniques are given in the following sections.

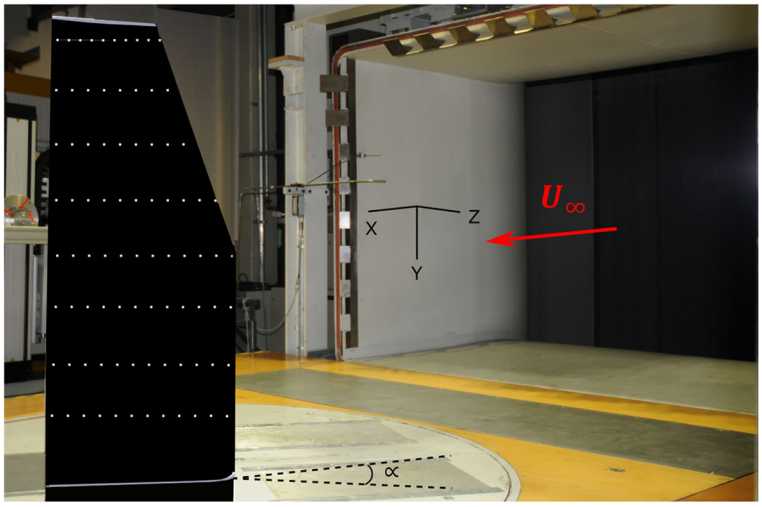

Fig. 2 Elasto-flexible membrane wing model mounted in the test section of wind tunnel A

3 Experimental procedures

3.1 Force measurements

An external six-components strain gauge balance is used to measure the aerodynamic forces and moments of the wing. The balance is set under the wind-tunnel test section floor. As the balance is connected to the wing, the extension of the strain gauge resulting from the aerodynamic loading renders the forces on it.

Force measurements are performed at several α for various freestream dynamic pressures q_∞. Table 1 gives an overview of the tests carried out in the wind tunnel with the associated conditions. As mentioned in Section 2, a circular plate allows to set α. The balance turns with the model, providing forces and moments in the wing-fixed coordinate system. Therefore, a rotation of α is mandatory to obtain the forces in the wind-tunnel coordinate system. Figure 3 illustrates the rotation transformation. The force measurements are recorded using a sampling frequency of 1 Hz averaged on a sampling time of 20 s. A repetition of the tests shows a maximum deviation in lift of $\Delta C_L = \pm 0.04$ and in drag of $\Delta C_D = \pm 0.004$.

3.2 Membrane deformation measurements

A stereo-photogrammetry technique is applied to measure the deflection of the wing. As the LE and TE are made of steel, an approximation of the deflection of the two spars was found to be less than 1% of the maximal membrane deformation. Consequently, the stereo-photogrammetry technique was employed to measure the membrane deformation. The procedure exploits the direct linear transformation (DLT) method to reconstruct the coordinates of specific pre-selected points. The points are marked with

Table 1 Summary of the different tests and measurement techniques

Flow condition	Force measurements	Deformation measurements
Re	4.35 x 10^5, 6.67 x 10^5, 8.70 x 10^5	4.35 x 10^5, 6.67 x 10^5, 8.70 x 10^5
q_∞	140 Pa, 310 Pa, 520 Pa	140 Pa, 310 Pa, 520 Pa
α	[-5 : 2 : 30] deg	-5 deg, 0 deg, 5 deg, 15 deg

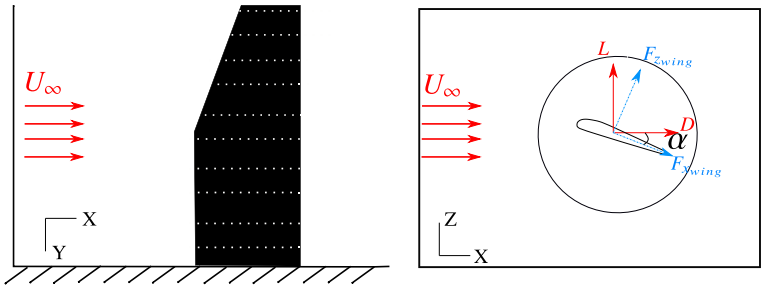

$$D = cos(\alpha)F_{x_{wing}} + sin(\alpha)F_{z_{wing}}$$
$$L = cos(\alpha)F_{z_{wing}} - sin(\alpha)F_{x_{wing}}$$

Fig. 3 Sketch explaining the rotation transformation for the force measurements

white reflectors. The points are set on the membrane and the measurements permit to reconstruct their coordinates. The basis of this method is illustrated in Fig. 4. One photo is taken by each of the two cameras placed at an angle of around 45 deg to one another. From the two photos, the equations of the DLT approach reconstruct the three dimensional coordinates of the reflectors.

A calibration is necessary to determine the unknown variables of the DLT method. A plane with a matrix of points, the distances of which are uniform and known, is used to calibrate the system. The plane is moved in the z-direction to calibrate a volume given by $[X_{min}\ X_{max},\ Y_{min}\ Y_{max},\ Z_{min}\ Z_{max}]$ as defined by the user. During the experiments, four cameras are used simultaneously to record both the upper and lower surface of the wing. The cameras have a resolution of 1600 x 1200 pixels, which in conjunction with the image optics and the distance to the model makes the area of the measured x-y plane 208 x 156 mm^2. One shot was not enough to record the whole wing in its length. Therefore, a translation in the y-direction was necessary to measure the deformation on the complete wing. Afterwards, an interpolation is used to obtain the deformation in all directions. Reconstruction of the position of the reference points during the calibration indicates an average accuracy of 0.13 mm per pixel.

3.3 Test conditions

The conducted measurements are summarized in Table 1. Force measurements are carried out for angles of attack from -5 deg to 30 deg for three freestream dynamic pressures, namely $q_\infty = 140$, 310 and 520 Pa. The membrane's deformation is measured for the same q_∞ but only at $\alpha = -5$, 0, 5, 10, and 15 deg.

4 Numerical procedures

The FSI computations are performed using two solvers: on the one hand, the TAU code is employed to resolve the Navier-Stokes equations and on the other hand, the CARAT++ code is employed to find the membrane deformation.

4.1 CFD and FEM solvers: TAU/CARAT++

4.1.1 CFD solver

The CFD code TAU from the DLR [18] solves the RANS equations governing the flowfield throughout the FSI computations. TAU can solve the equations either toward steady state or time-accurately for unsteady problems. A cell-vertex spatial scheme is employed to

perform the fluid computations and the multigrid method is furthermore exploited to accelerate solution convergence. A three level W-symmetric multigrid cycle is therefore selected. The coupling between TAU and the FEM solver is achieved through a Python code.

The computations are performed with a dual time step method and several physical time steps, namely 150, 300 and 600μs, are investigated to perform a time step sensitivity study. The URANS computations are based on the Spalart-Allmaras one-equation turbulence model assuming a fully developed turbulence boundary layer. Finally, the converged state at two angles of attack, namely $\alpha = 5$ deg and $\alpha = 10$ deg for $q_\infty = 520$ Pa, are investigated and compared to the experimental data to assess the accuracy of the computations.

4.1.2 FEM solver

The equations governing the displacement of the membrane are solved with the CARAT++ code [19]. The dislocation of the structure is calculated in an incremental way based on the principle of solution advancement by continuation. The procedure starts with the unloaded structure and converges to an equilibrium solution under a load distribution by advancing the solution step by step. In the current study, a predictor-corrector method using force control is used to solve the structural problem. In predictor-corrector methods, iterations are performed to calculate the new equilibrium state.

The membrane deformation is modeled with membrane element. The material is 0.5 mm and has a mass per surface area of 160 g/m^2. The ratio between the thickness of the membrane and the root chord length or the span is found to be smaller than 10^{-3}. Therefore all stresses in the thickness direction can be assumed to be negligible. Elements on the LE and the TE are fixed to keep the geometry of the section according to what was found in the experiments. Furthermore, the wing root, the wing tip and the peniche are considered as fixed bodies as well to be consistent with the experimental procedure. The elements on the membrane are allowed to dislocate in all the spatial directions. An initial pre-stress of $\sigma_{01} = 2.1$ MPa is set for the membrane in the chord direction just as in the experiments. An additional pre-stress of $\sigma_{02} = 0.4$ MPa is set in the span direction to avoid possible surface crinkles. Furthermore, the membrane is assumed to be anisotropic with an elasticity modulus of $E = 4$ MPa and a Poisson coefficient of $\nu = 0.2$.

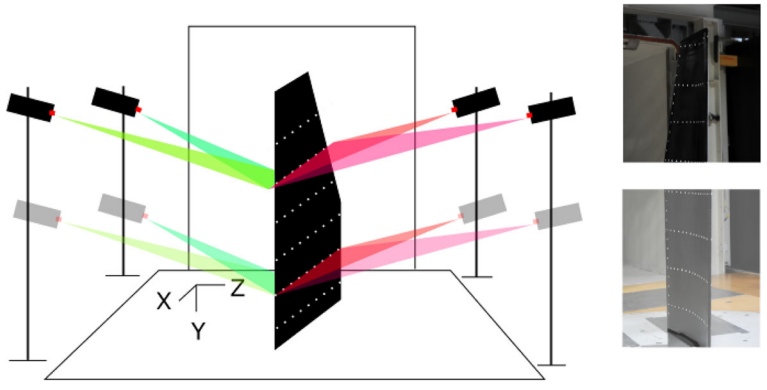

Fig. 4 Sketch explaining the two operations during a photogrammetry measurement

4.1.3 FSI coupling

The open-source coupling tool EMPIRE [22] realizes the coupling of CARAT++ and TAU. Two clients are involved in the FSI simulations. The fluid client starts by solving the flow problem and then sends the local forces on the membrane to EMPIRE. Next, EMPIRE performs the mapping between the CFD and FEM surfaces and transfers the forces to the structural client. Afterwards, CARAT++ renders the displacement and transfers it back to EMPIRE. Finally, the fluid client receives the displacement through the mesh mapping. The coupling iteration ends by applying the displacement to the CFD mesh. Coupling iterations are repeated until convergence is reached.

The mapping itself is executed by using a modified dual-mortar mapping method for the force exchange and a nearest-element method for the displacement transfer [22]. On the one hand, the mortar mapping is based on consistency, implying that an invariant field is exactly mapped from one mesh to the other. It also uses the principle of energy conservation: The total energy is conserved as the fields are mapped between the meshes at the interface. The modified dual mortar method enforces consistency of the mapping by scaling up the structural shape functions. On the other hand, in the displacement mapping with the nearest-element interpolation, each fluid node is projected onto its nearest element in the structure mesh and the unknown value of the displacement is assigned as a result of interpolating the projection node inside the element.

4.2 Meshes

Two different meshes are necessary for the computations. One for the URANS computations and one for the FEM analysis. Each mesh is of a structured type, albeit obtained with a separate grid generator. The CFD mesh is constructed by means of ICEM CFD [23], while the structural mesh is constructed with GiD [24].

4.2.1 CFD mesh

The flowfield is globally discretized using a C-topology mesh. An O-topology, however, is employed to refine the wing's near field, ensuring a more accurate resolution of the boundary layer. A detailed overview of the computational domain and the grid is given in Fig. 5. The mesh is generated with a resolution of $y^+ < 1$ near the wing. The growth ratio of the cell in the wall-normal layer is lower than 1.2. Finally, a minimum cell angle of 30 deg is achieved to ensure a good quality of the mesh. The computational domain has a size of 20 x c_{max} in the freestream direction behind the wing and 12 x c_{max} in the other directions. Far-field boundary conditions are prescribed at the inflow; the wind-tunnel floor as well as the wing and the peniche wall are modelled with a turbulent viscous wall.

A grid-sensitivity study is conducted to ensure the results independency from the spatial discretization. Three distinct resolutions are investigated; their characteristics are summarized in Table 2. The grid sensitivity is performed for two angles of attack, namely $\alpha = 5$ deg and $\alpha = 10$ deg. The results are summarized in Table 3 where C_L and C_D are described. The coefficients are fluctuating for the coarse mesh whereas they achieved a constant value for the two finer resolutions. The deviation of C_L between the medium and the fine CFD mesh (the values for the medium mesh are used as references) is equal to 0.2% at $\alpha = 5$ deg and to 0.1% at $\alpha = 10$ deg, and the deviation of C_D is equal to 1.6% at $\alpha = 10$ deg. As a compromise with respect to computational effort and accuracy enhancement, the medium resolution is chosen for the FSI computations.

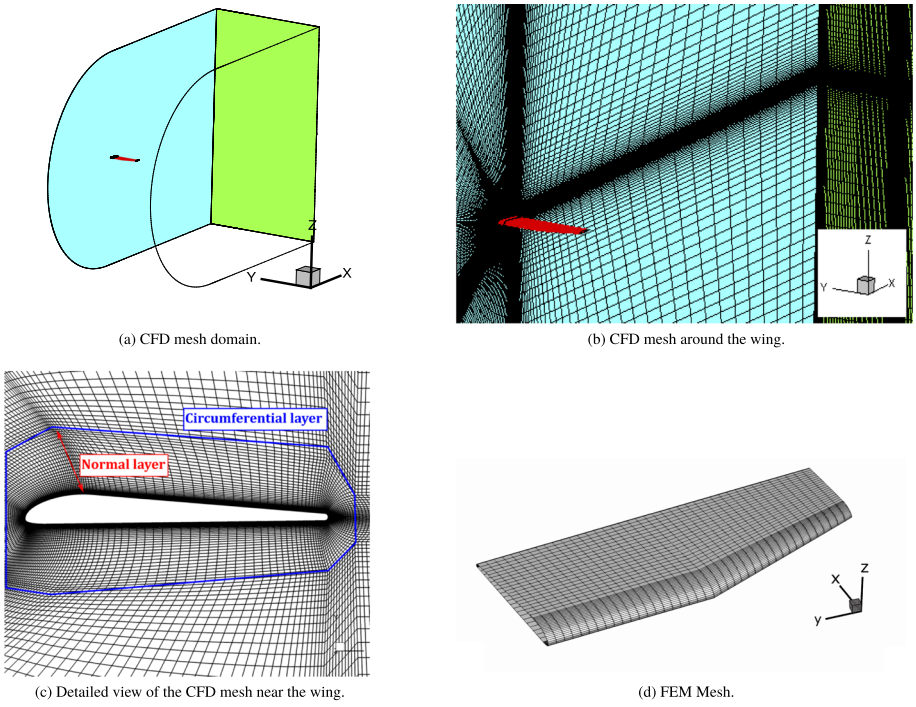

(a) CFD mesh domain.

(b) CFD mesh around the wing.

(c) Detailed view of the CFD mesh near the wing.

(d) FEM Mesh.

Fig. 5 CFD and FEM Meshes. **a** CFD mesh domain. **b** CFD mesh around the wing. **c** Detailed view of the CFD mesh near the wing. **d** FEM Mesh

A time-step sensitivity study is performed as well. The preliminary physical time step is equal to $\delta t = 300\,\mu s$. The time step analysis is performed by studying the response of the computations for the half and the double of $\delta t = 300\,\mu s$. The results show that for $\delta t = 300\,\mu s$ and $\delta t = 600\,\mu s$, C_L and C_D are the same. However, for $\delta t = 150\,\mu s$, undesired unsteady phenomena occur. Consequently, the time step of $\delta t = 600\,\mu s$ is chosen for the following computations.

4.2.2 FEM mesh

The FEM mesh is generated with GiD [24]. It is an adaptive pre- and post-processor for numerical computations developed at the International Centre for Numerical Methods in Engineering (CIMNE). The structured mesh with quadrilateral elements is shown in Fig. 5. Analogously to the CFD mesh, a refinement study is performed to ensure the results independency of the spatial discretization. The study is performed by applying a pressure load to the membrane of the same order of magnitude as the expected pressure loads in the FSI computations. Four different meshes were investigated. Between two resolutions, 10 nodes are added in each line of the chord direction. As the error between the resolutions does not exceed 0.1%, the selected mesh is the one with 4100 nodes (20

Table 2 Characteristics of the different resolutions of the grids

Characteristics	Coarse	Medium	Fine
Total numbers of nodes	4.6 Million	8.9 Million	12.3 Million
Normal layer nodes	54 elements	65 elements	90 elements
Circumferential layer nodes	244 elements	244 elements	244 elements

Table 3 Comparison of the lift and drag coefficients between the different spatial resolutions at $\alpha = 5$ deg and $\alpha = 10$ deg

-	Coarse	Medium	Fine
C_L at $\alpha = 5$ deg	0.519 ±0.027	0.516	0.515
C_D at $\alpha = 5$ deg	0.032 ±0.003	0.029	0.029
C_L at $\alpha = 10$ deg	0.906 ±0.026	0.898	0.897
C_D at $\alpha = 10$ deg	0.066 ±0.005	0.063	0.062

nodes per line) and presents a relative error of 0.05% in comparison with the finest resolution. A finer mesh is generated at the LE and TE to capture the geometry accurately. Although these areas do not contribute to the structural loading, an accurate representation of the geometry is necessary to ensure the correct coupling between the CFD mesh and the FEM mesh.

5 Results and discussion

5.1 Benefits of an elasto-flexible lifting surface

Before presenting the results obtained during this analysis, a brief introduction is given on the effects of the membrane as lifting surface of a wing. Previous investigations [25, 26] show that the membrane flexibility and adaptivity allow a passive flow control. The membrane enables a change of the surface contour under a varying dynamic pressure permitting a change in the airfoil's camber. When the elasto-flexible geometry is compared to its rigid counterpart, the camber increase leads to higher C_L. Furthermore, the stall region of the wing is modified. Instead of having an abrupt decrease of C_L, the lift slope $C_{L\alpha}$ becomes shallower causing a gradual decrease of C_L. Therefore, the onset of stall is delayed to higher angles of attack and the stall occurs smoothly. In the following, the results obtained for the three-dimensional model are presented in two sections. On the one hand, the aerodynamic parameters (C_L and C_D) and the membrane deflection are plotted at various dynamic pressures and on the other hand, FSI data are compared to the experiments values.

Dynamic-Pressure Dependency: Lift, Drag and Lifting Surface Deflection

The following data are obtained for the experimental three-dimensional flexible wing shown in Fig. 1. The wind-tunnel test data are depicted in Fig. 6, namely C_L-α and C_L-C_D for three dynamic pressures: $q_\infty = 140$ Pa, $q_\infty = 310$ Pa and $q_\infty = 520$ Pa. In Fig. 7, the membrane dislocation is depicted along the span. All parameters C_L, C_D and the membrane deflection have to be analyzed and compared to understand the features of the flexible wing concept.

For a low q_∞, namely 140 Pa, C_L increases linearly with α until it reaches $C_{L-max} \simeq 1.3$ at $\alpha = 15$ deg. Then, C_L decreases gradually up to $\alpha = 15$ deg suggesting the progression of the flow separation to the LE. Fig. 7 illustrates the membrane dislocation. At $\alpha = 0$ deg and $\alpha = 5$ deg, the dislocation of the membrane is quasi-null: The pressure induced on the membrane at $q_\infty = 140$ Pa is not sufficient against the membrane tension to cause a dislocation. At $\alpha = 10$ deg a dislocation of both membrane sides appears at -0.11 m and -0.74 m of the spanwise but is too small to influence the linearity of C_L-α. At $\alpha = 15$ deg, the lower surface of the membrane dislocates to the z-axis direction resulting from the pressure side, whereas the upper surface dislocates lightly to *(-z)*-axis direction (Fig. 7 at -0.74 m and -0.11 m of the spanwise). The latter is caused by the flow separation starting

at the TE and progressing to the LE inducing a pressure less favorable to the dislocation. At $q_\infty = 140$ Pa, the wing can be compared to a rigid wing in the linear part and the aerodynamic characteristics, namely C_L-α and C_L-C_D can be used as reference data for the following.

$C_{L\alpha}$ shows a pronounced dependency on q_∞. For higher q_∞, namely 310 Pa and 520 Pa, $C_{L\alpha}$ becomes steeper than for $q_\infty = 140$ Pa in the linear region of the C_L-α curve, i.e., between $\alpha = -5$ deg to $\alpha = 15$ deg. The latest is due to the change of the wing's camber. The airfoil-section's camber increases with q_∞ and α compared to the case $q_\infty = 140$ Pa as the pressure distribution on the membrane upper side surface increases with both parameters. C_L reaches higher values at every α for both $q_\infty = 310$ and 520 Pa. The curve C_L-C_D shows the same efficiency in the linear region, which indicates that C_D increases with q_∞ at a same α as well. Furthermore, in the stall region, i.e., between $\alpha = 15$ deg to $\alpha = 30$ deg, C_L is higher for higher q_∞, which suggests that the flexibility of the membrane allows also a higher camber in the stall region.

5.2 Evaluation of the accuracy of the computations

The numerical computations are compared to experimental data for cross-evaluation. In the following, a comparison at $\alpha = 5$ deg and $\alpha = 10$ deg for $q_\infty = 520$ Pa is performed between FSI computations and wind tunnel tests. On the one hand, C_L-α and C_D-α are compared on Fig. 8. On the other hand, the deflection of the membrane is plotted in Fig. 9.

The FSI computations were performed as described in Section 4.1.3. The coupling is computed till the aerodynamic coefficients converge. The maximal error of C_L and C_D between the two latest iterations are equal to 0.35% and 0.4%, respectively. On the one hand, the FSI computations estimate $C_L = 0.85$ and $C_D = 0.059$ at $\alpha = 5$ deg, whereas $C_L = 0.92$ and $C_D = 0.079$ are measured at $\alpha = 5$ deg in the wind tunnel. A difference between FSI computations and wind tunnel data is of 7% and 25% for C_L and C_D, respectively. On the other hand, $C_L = 1.18$ and $C_D = 0.124$ are predicted at $\alpha = 10$ deg, whereas the wind tunnel tests measured $C_L = 1.11$ and $C_D = 0.113$ at $\alpha = 9$ deg and $C_L = 1.18$ and $C_D = 0.130$ at $\alpha = 11$ deg: the difference between FSI computations and wind tunnel data are under 6.2% and 9% for C_L and C_D, respectively.

The FSI computations show a good agreement with the wind-tunnel data. Nevertheless, the small differences obtained in C_L and C_D at $\alpha = 5$ deg and $\alpha = 10$ deg can be

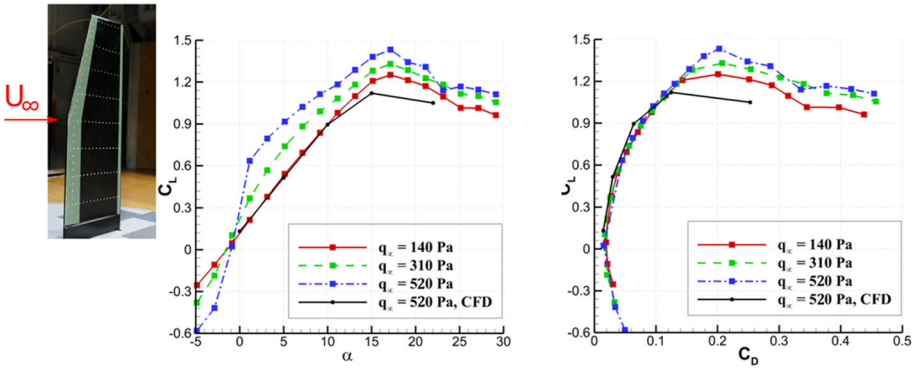

Fig. 6 Evolution of C_L-α and C_L-C_D obtained with the experiments at three q_∞ and with CFD computations at $q_\infty = 520$ Pa

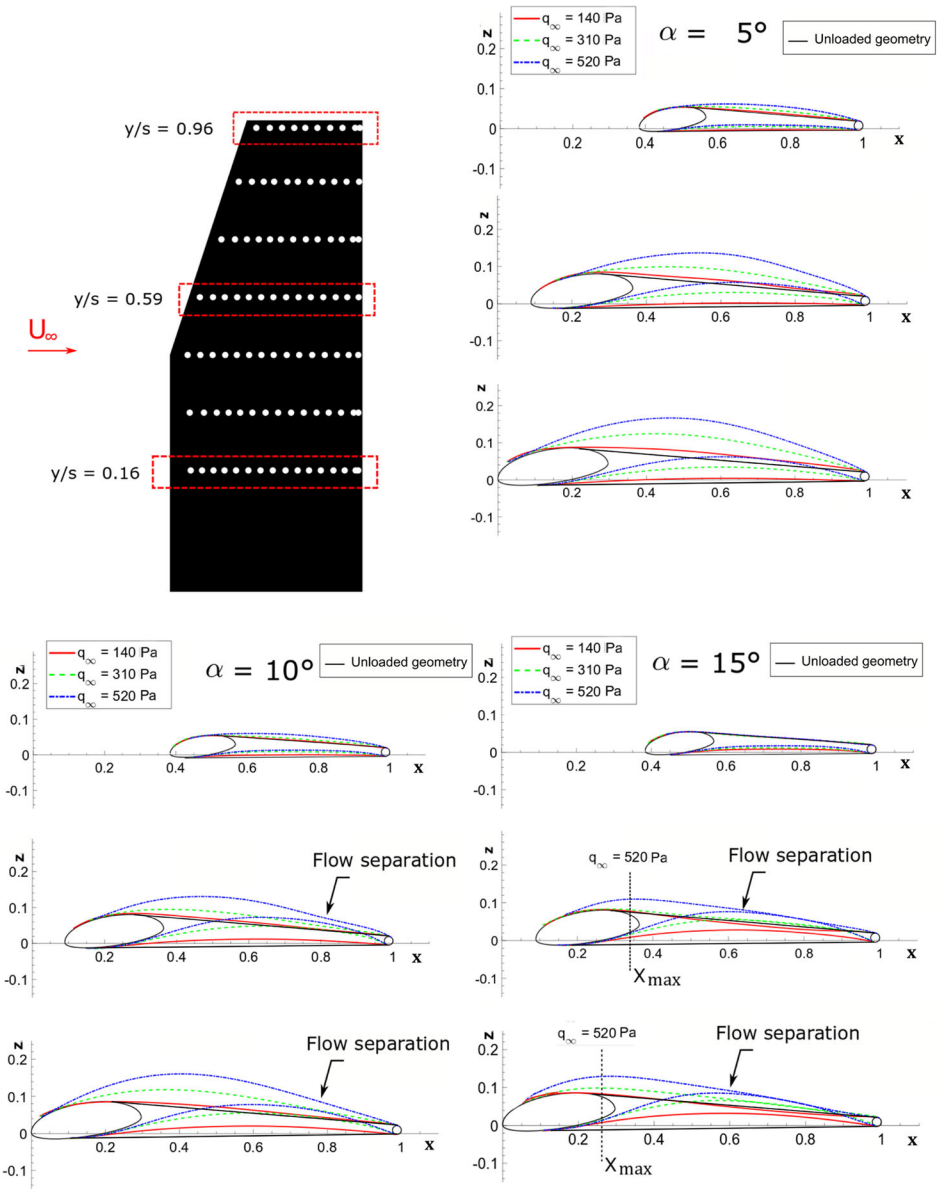

Fig. 7 Membrane deflection at $\alpha = 5$, 10 and15 deg and $q_\infty = 140$, 310 and 520 Pa

explained by analyzing the membrane deflection described in Fig. 9. The figure shows the membrane deflection for three sections in the spanwise direction and compared the FSI results to the experimental data. At $\alpha = 5$ deg, the membrane deflection is well estimated at $y/s = 0.16$ but a higher disparity is observed at $y/s = 0.592$ on both surfaces. The FSI computations underestimates the membrane deflection at $y/s = 0.592$ explaining the discrepancy in C_L and C_D observed in the polar curves of Fig. 8. At $y/s = 0.96$, small disparities are observed as well. At $\alpha = 10$ deg, the membrane deflection is well estimated on the upper-side surface of the membrane at $y/s = 0.16$ and $y/s = 0.592$, whereas small differences are observed at $X = 0.8$ on the lower-side surface at $y/s = 0.592$. Nevertheless, a good agreement is obtained for the membrane deflection, resulting in a good agreement in C_L and C_D.

6 Conclusion

The flexibility and the adaptivity of a membrane serving as a lifting surface have been analyzed with fluid-stucture-interaction simulations by means of the TAU code and the FEM CARAT++ solver. The lift and drag coefficients of the flexible geometry are compared to the values obtained for the rigid counterpart. The simulations are validated with wind-tunnel data by comparing the aerodynamic coefficients and the membrane deflection at various angles of attack. The wind-tunnel data were also performed for three distinct Reynolds numbers at various angles of attack. The aerodynamic coefficients are analyzed to draw conclusions about the dependency of the flexible geometry to the dynamic pressure.

Regarding the benefits of the flexible geometry, the membrane adjusts its shape to the pressure distribution. The flexibility and adaptivity of the material allow a change of the wing geometry, which can positively influence a lift increase. At small angles of attack, a positive membrane deflection and an increase in the airfoil's camber are observed. The gradient of pressure is higher than for the rigid geometry over a broader wing area, which enables the lift to be higher than for the rigid geometry. At higher angles of attack, the onset of stall is postponed and the abrupt decrease of the lift is replaced by a gradual decrease of it. The flexible geometry offers a better aerodynamic efficiency in the stall region than its rigid counterpart. Furthermore, the wind tunnel data show that the lift and the lift slope have a pronounced dependency on the dynamic pressure. Both increase with it at small angles of attack as the membrane deflection leads to a higher camber. The gradual decrease of the lift for high angles of attack still occurs at various dynamic pressures and is also delayed. Concerning the fluid-structure-interaction simulations, they show a good agreement with the wind tunnel data and suggest, therefore, good promises in the development of accurate high-fidelity computations.

Nomenclature

Re Reynolds number

q_∞ freestream dynamic pressure, Pa

E_1, E_2, E Moduli of elasticity in the warp and the weft directions of the membrane and taken for the computations, MPa

a_1, a_2 dimensionless value of the prior axis of the ellipse at the root and at the tip, respectively

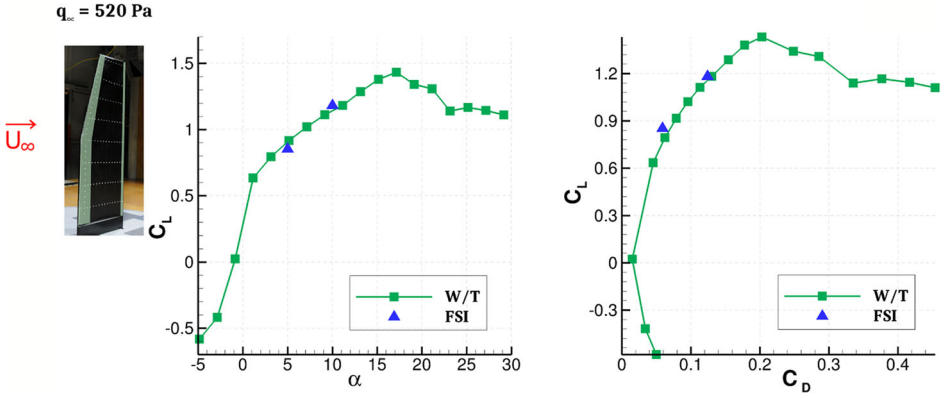

Fig. 8 Comparison of C_L-α and C_L-C_D for FSI and wind tunnel data at $q_\infty = 520$ Pa

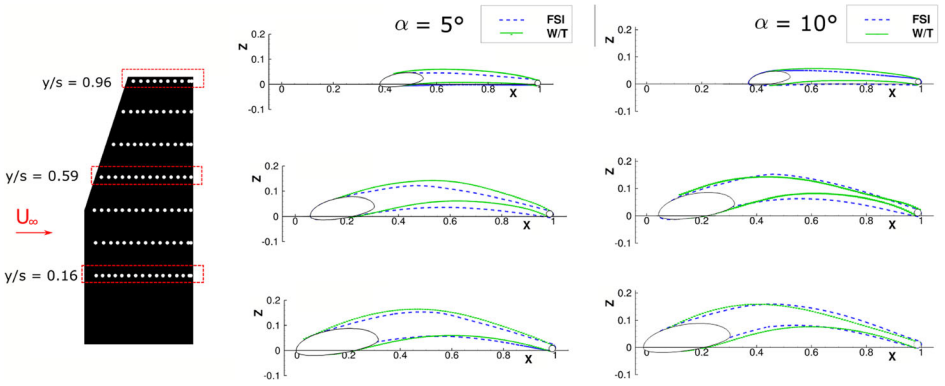

Fig. 9 Evolution of the deformation along the wing issued from the FSI computations and the experiments at $\alpha = 5$ deg and 10 deg and $q_\infty = 520$ Pa

b_{u1}, b_{u2} dimensionless value of the second axis of the upper half ellipse at the root and at the tip, respectively

b_{l1}, b_{l2} dimensionless value of the second axis of the lower half ellipse at the root and at the tip, respectively, -

d_{te} dimensionless value of the diameter of the trailing edge

s span of the wing, m

S reference area of the wing, m^2

AR aspect ratio of the wing

λ taper ratio of the wing

c chord length, m

x, y, z wind-tunnel coordinates

X, Y, Z dimensionless wind-tunnel coordinates related to the root chord

X_{max} dimensionless coordinate for the maximal deformation of the membrane

U_∞ freestream velocity, ms^{-1}

u, w axial and vertical velocity, ms^{-1}

C_l, C_L lift coefficient for airfoil and wing, respectively

$C_{L\alpha}$ slope of the lift curve over α

C_d, C_D drag coefficient for airfoil and wing, respectively

α angle of attack, deg

α_0 angle of attack for $C_L = 0$, deg

$\alpha_{C_{L-max}}$ angle of attack for maximal C_L, deg

C_P pressure coefficient

Abbreviations

CFD: Computational fluid dynamic; *DLR*: German Aerospace Center; *DLT*: Direct linear transformation; *FEM*: Finite-element method; *FSI*: Fluid-Structure-Interaction; *LE*: Leading edge; *MAV*: Micro air vehicle; *RANS*: Reynolds-averaged-Navier-Stokes; *TE*: Trailing edge; *TUM-AER*: Chair of Aerodynamics and Fluid Mechanics at Technical University of Munich; *TUM-SA*: Chair of Structural Analysis at Technical University of Munich

Acknowledgements

The authors would like to thank the German Research Association for the funding of the project BR 1511/10-1. Furthermore, the authors thank the German Aerospace Center (DLR) for providing the DLR TAU-Code and for their support. The authors gratefully acknowledge the Gauss Center for Supercomputing e.V. for funding this project by providing computing time on the Gauss Center for Supercomputing's Supercomputer SuperMUC at Leibniz Supercomputing Center. Further thanks are given to ANSYS, Inc. for providing the mesh generator software. Finally, the authors express a profound gratitude to the Technische Universität München Graduate School's Faculty Graduate Center of Mechanical Engineering.

Authors' contributions
JP conducted the wind tunnel investigations and performed the numerical fluid-structure-interaction computations. JP contributed to the development of the fluid part of the computations whereas IL contributed to the structural part. All authors contributed to the analysis of the results and the finalization of the script. All authors read and approved the final manuscript.

Funding
The authors would like to thank the German Research Association for the funding of the project BR 1511/10-1.

Availability of data and materials
The datasets used and/or analysed during the current study are available from the corresponding author on reasonable request.

Competing interests
The authors declare that they have no competing interests.

Received: 18 July 2019 Accepted: 4 November 2019
Published online: 20 December 2019

References

1. Weisshaar TA (2013) Morphing Aircraft Systems: Historical Perspectives and Future Challenges. J Aircr 50(2):337–353. https://doi.org/10.2514/1.C031456
2. Vasista S, Tong L, Wong KC (2012) Realization of Morphing Wings: A Multidisciplinary Challenge. J Aircr 49(1):11–28. https://doi.org/10.2514/1.C031060
3. Rodriguez A (2007) Morphing Aircraft Technology Survey, Aerospace Sciences Meetings, American Institute of Aeronautics and Astronautics, Reno. https://doi.org/10.2514/6.2007-1258
4. Moorhouse D, Sanders B, Spakovsky Mv, Butt J (2016) Benefits and design challenges of adaptive structures for morphing aircraft. Aeronaut J 110(1105):157–162. https://doi.org/10.1017/S0001924000001135
5. Flanagan J, Strutzenberg R, Myers R, Rodrian J (2007) Development and Flight Testing of a Morphing Aircraft, the NextGen MFX-1, Structures, Structural Dynamics, and Materials and Co-located Conferences, American Institute of Aeronautics and Astronautics, Honolulu. https://doi.org/10.2514/6.2007-1707
6. Hu H, Tamai M, Murphy JT (2008) Flexible-Membrane Airfoils at Low Reynolds Numbers. J Aircr 45(5):1767–1778. https://doi.org/10.2514/1.36438
7. Yokozeki T, Sugiura A, Hirano Y (2014) Development of Variable Camber Morphing Airfoil Using Corrugated Structure. J Aircr 51(3):1023–1029. https://doi.org/10.2514/1.C032573
8. Ifju P, Jenkins D, Ettinger S, Lian Y, Shyy W, Waszak M (2002) Flexible-wing-based micro air vehicles, Aerospace Sciences Meetings, American Institute of Aeronautics and Astronautics, Reston. https://doi.org/https://doi.org/10.2514/6.2002-705
9. Stanford B, Viieru D, Albertani R, Shyy W, Ifju P (2006) A Numerical and Experimental Investigation of Flexible Micro Air Vehicle Wing Deformation, 44th AIAA Aerospace Sciences Meeting and Exhibit, American Institute of Aeronautics and Astronautics, Reno. https://doi.org/10.2514/6.2006-440
10. Campanile LF, Sachau D (2000) The Belt-Rib Concept: A Structronic Approach to Variable Camber. J Intell Mater Syst Struct 11(3):215–224. https://doi.org/10.1106/6H4B-HBW3-VDJ8-NB8A
11. Woods BKS, Dayyani I, Friswell MI (2014) Fluid/Structure-Interaction Analysis of the Fish-Bone-Active-Camber Morphing Concept. J Aircr 52(1):307–319. https://doi.org/10.2514/1.C032725
12. Barlas TK, van Kuik G (2010) Review of state of the art in smart rotor control research for wind turbines. Progress Aerosp Sci 46(1):1–27. https://doi.org/10.1016/j.paerosci.2009.08.002
13. Bak C, Gaunaa M, Andersen P, Buhl T, Hansen P, Clemmensen K, Moeller R (2007) Wind Tunnel Test on Wind Turbine Airfoil with Adaptive Trailing Edge Geometry, 45th AIAA Aerospace Sciences Meeting and Exhibit, American Institute of Aeronautics and Astronautics, Reno. https://doi.org/10.2514/6.2007-1016
14. Troldborg N (2005) Computational Study of the Risø-B1-18 Airfoil with a Hinged Flap Providing Variable Trailing Edge Geometry. Wind Eng 29(2):89–113. https://doi.org/10.1260/0309524054797159
15. Chow R, van Dam C (2007) Computational Investigations of Deploying Load Control Microtabs on a Wind Turbine Airfoil, Reno, 45th AIAA Aerospace Sciences Meeting and Exhibit, American Institute of Aeronautics and Astronautics, Reno. https://doi.org/10.2514/6.2007-1018
16. Baker J, Standish K, van Dam C (2005) Two-Dimensional Wind Tunnel and Computational Investigation of a Microtab Modified S809 Airfoil, 43rd AIAA Aerospace Sciences Meeting and Exhibit, American Institute of Aeronautics and Astronautics, Reno. https://doi.org/10.2514/6.2005-1186
17. De Gaspari A, Ricci S (2011) A Two-Level Approach for the Optimal Design of Morphing Wings Based On Compliant Structures. J Intell Mater Syst Struct 22(10):1091–1111. https://doi.org/10.1177/1045389X11409081
18. Gerhold T (2005) Overview of the Hybrid RANS Code TAU, MEGAFLOW - Numerical Flow Simulation for Aircraft Design(Kroll N, Fassbender JK, eds.). Springer Berlin Heidelberg
19. Chair of Structural Analysis TUM (2018) Carat++. http://carat.st.bv.tum.de. Accessed 27 Nov 2019
20. Beguin B (2014) Development and analysis of an elasto-flexible morphing wing. Dissertation, Technische Universität München, München
21. Béguin B, Breitsamter C, Adams N (2012) Aerodynamic Investigations of a Morphing Membrane Wing. AIAA J 50(11):2588–2599. https://doi.org/10.2514/1.J051772
22. Wang T (2016) Development of Co-Simulation Environment and Mapping Algorithms. Dissertation, Technische Universität München, München
23. ANSYS (2012) ANSYS ICEM CFD User Manual. https://pdfs.semanticscholar.org/c728/37a63921bbc47c83fa3d6bad8e2d9a86e2f7.pdf. Accessed 27 Nov 2019

24. Coll A, Ribó R, Pasenau M, Escolano E, Perez J, Melendo A, Monros A, Gárate J (2016) GiD v.13 User Manual. https://www.gidhome.com/support/gid-manuals/. Accessed 27 Nov 2019
25. Piquee J, López I, Breitsamter C, Wüchner R, Bletzinger K-U (2018) Aerodynamic Characteristics of an Elasto-Flexible Membrane Wing based on Experimental and Numerical Investigations. In: 2018 Applied Aerodynamics Conference. American Institute of Aeronautics and Astronautics, Reston. https://doi.org/10.2514/6.2018-3338
26. Piquee J, Breitsamter C (2017) Numerical and Experimental Investigations of an Elasto-Flexible Membrane Wing at a Reynolds Number of 280,000. Aerospace 4(3):39. https://doi.org/10.3390/aerospace4030039

Publisher's Note